Effect of Spherical Wavefronts on Very-High-Frequency (VHF) Lightning Interferometer Observations

Xiangpeng Fan[®], Paul R. Krehbiel[®], Mark A. Stanley, Yijun Zhang[®], William Rison[®], and Harald E. Edens[®]

Abstract—Interferometric measurements of very-highfrequency (VHF) radio frequency signals produced by lightning are one of the most effective techniques for studying lightning breakdown processes, so uncertainty and error analyses of interferometric location results have become important topics. Based on the plane wave approximation of lightning RF signal transmission for interferometric location, a geometric model for the systematic error in the interferometric location due to the wavefront being spherical is developed and evaluated for short baseline interferometers, beginning with orthogonal and equilateral triangle baseline layouts. The symmetry of the baseline layout is shown to be helpful for reducing the systematic error caused by the plane wave approximation in interferometric location using a geometric relationship. Furthermore, a baseline layout scheme with the center of an equilateral triangle as the coordinate origin optimizes the systematic error caused by the plane wave approximation.

 ${\it Index Terms} \hbox{--Lightning observation, very-high-frequency (VHF) lightning interferometer.}$

I. INTRODUCTION

INTERFEROMETRIC measurements of very-high-frequency (VHF) radio frequency signals radiated by lightning are one of the most effective techniques for studying the lightning breakdown process. Interferometry based on narrowband signal detection was first introduced to research on lightning observation and lightning physics during

Manuscript received 14 June 2023; revised 26 September 2023; accepted 3 November 2023. Date of publication 7 November 2023; date of current version 17 November 2023. This work was supported in part by the National Science Foundation under Grant AGS 1720600 and Grant 2214044, in part by the National Natural Science Foundation of China under Grant 42175090, in part by the China Postdoctoral Science Foundation under Grant 2020M670974, and in part by the Gansu Science and Technology Program under Grant 18JR2RA005. (Corresponding author: Xiangpeng Fan.)

Xiangpeng Fan is with the Department of Plateau Atmospheric Physics, Northwest Institute of Eco-Environment and Resources, Chinese Academy of Sciences, Lanzhou, Gansu 730000, China, also with the Pingliang Land Surface Process and Severe Weather Research Station, Chinese Academy of Sciences, Gansu Land Surface Process and Severe Weather Observation and Research Station, Pingliang, Gansu 744015, China, and also with the Langmuir Laboratory for Atmospheric Research, Geophysical Research Center, New Mexico Institute of Mining and Technology, Socorro, NM 87801 USA (e-mail: fanxp04@gmail.com).

Paul R. Krehbiel, Mark A. Stanley, William Rison, and Harald E. Edens are with the Langmuir Laboratory for Atmospheric Research, Geophysical Research Center, New Mexico Institute of Mining and Technology, Socorro, NM 87801 USA (e-mail: krehbiel@ibis.nmt.edu; sparky@mark-stanley.name; rison.bill@gmail.com; harald.edens@nmt.edu).

Yijun Zhang is with the Department of Atmospheric and Oceanic Sciences and the Institute of Atmospheric Sciences, Fudan University, Shanghai 200438, China (e-mail: zhangyijun@fudan.edu.cn).

Digital Object Identifier 10.1109/TGRS.2023.3330899

the 1980s [1], [2], [3], [4]. Under the technical constraints at that time, the interferometers were analog systems and utilized measurements of phase differences between long and short orthogonal baselines to determine the 2-D source directions. Observations acquired in this fashion facilitated early endeavors to detect and study lightning, improving our understanding of the basic structural characteristics of lightning phenomena [5], [6], [7], [8], [9].

The rapid growth of high-speed digital and computerbased data acquisition and recording technologies has enabled the continued development of interferometer-based lightning detection systems. Particularly important has been the development of broadband techniques, first introduced into the field of lightning studies by Shao et al. [10]. Compared with narrowband systems, broadband interferometry greatly simplifies the antenna array structure and front-end RF electronics, avoids ambiguity in the source direction, and provides more accurate lightning discharge information. Consequently, these systems have been used extensively and have undergone rapid development. Due to recording limitations, broadband observations were initially obtained in a succession of microsecond-duration time segments spread out over entire flashes utilizing digital storage oscilloscope technology, with the source directions determined from the phase difference versus frequency for pairs of receiving antennas within each segment [11], [12], [13], [14], [15]. Eventually, due to the development of increasingly large data storage capabilities and fast transfer rates, it became possible to record flashcontinuous data. This allowed cross correlation techniques to be used to accurately determine time differences of arrival (TDOAs) between pairs of antennas and the 2-D azimuth and elevation source arrival directions [16], [17], [18]. The result has been major advances in discovering and understanding lightning discharge processes, obtained utilizing orthogonal baseline systems [19], [20], [21], [22], [23] and at the same time triangular configurations [24], [25], [26].

With the development of broadband interferometry, the location accuracy and spatiotemporal resolution of lightning discharge processes have constantly been improving. Nevertheless, uncertainty and error analyses of interferometric location have remained very important topics. Based on Carter's [27] lower bound uncertainty formula, Stock et al. [16] and Stock [17] presented an uncertainty analysis for their interferometer observations of coherent time delay estimates. More recently, Shao et al. [28] analyzed the influence of the

1558-0644 © 2023 IEEE. Personal use is permitted, but republication/redistribution requires IEEE permission. See https://www.ieee.org/publications/rights/index.html for more information.

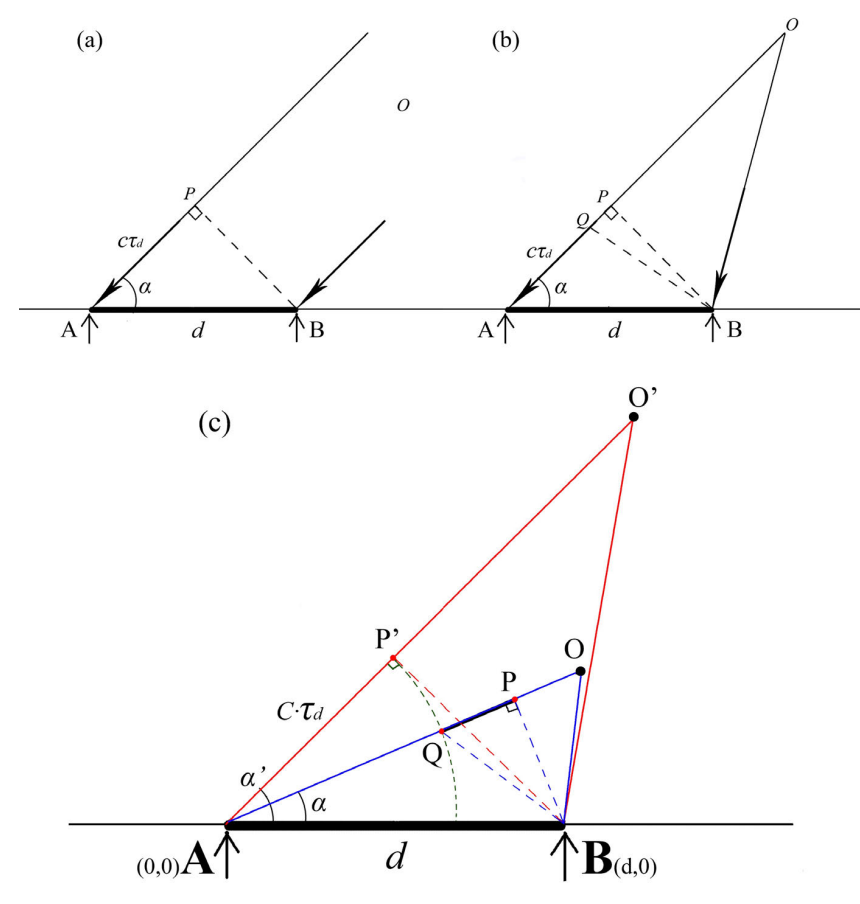


Fig. 1. (a) Plane wave model. (b) Spherical wave model. (c) Illustration of how a source at point O (blue lines) appears to be at a higher angle α' (red lines) for a given TDOA $c \cdot \tau_d$ (dashed arc). Note that neither α nor α' is the elevation angle of the radiation source; rather, these are the angles between the plane of the radiation source and the baseline.

time delay error between windows on the location uncertainty based on a cross correlation time delay estimation, which constitutes the basis of the broadband interferometric location technology. In addition, a beam steering technique was proposed to improve the broadband interferometric mapping capability and to more reliably estimate the mapping uncertainties/errors for individual lightning sources. However, no studies have addressed the effect of utilizing the plane wave approximation on the location accuracy, which causes systematic errors for close flashes and for increasing baseline lengths.

In this study, we review the formulations of the plane wave approximation for short-baseline lightning interferometers and present a geometric model of the systematic error caused by the use of the plane wave approximation. Subsequently, the characteristics of interferometers utilizing orthogonal and triangular three-antenna configurations are analyzed using numerical simulations. The results show that the errors are reduced not only by the improved symmetry of triangular configurations but also surprisingly by the coordinate origin being symmetrically placed.

II. ERROR SOURCE ANALYSIS AND SIMULATION METHOD A. Plane Wave Model

The basic geometry of the plane wave model for locating the source arrival direction is illustrated in Fig. 1(a). For distant lightning sources compared to the antenna spacing d, the incidence angle of the signal arriving at two receiving antennas A

and B is approximately the same, α . For a given arrival TDOA τ_d at the two antennas, the cosine of the incident angle is determined from

$$d\cos\alpha = c\tau_d \tag{1}$$

where c is the speed of light in air. When three antennas are situated along orthogonal x and y baselines (AB and AC, one of which points north and defines the azimuth angle as increasing clockwise from north), the incident angles of the signals generated by radiation source at point O arriving at baselines AB and AC are α and β , respectively, and the TDOAs determine the direction cosines of the source in spherical geometry. From spherical trigonometry [5], [16], the direction cosines are related to the azimuth (Az) and elevation (El) of the source by

$$\cos \alpha = \sin(\text{Az})\cos(\text{El})$$

 $\cos \beta = \cos(\text{Az})\cos(\text{El}).$ (2)

The above expressions can be inverted to obtain the azimuth and elevation in terms of the two TDOAs, τ_{d1} and τ_{d2} , yielding the following:

Az =
$$\arctan\left(\frac{\tau_{d1}}{\tau_{d2}}\right)$$

El = $\arccos\left(\frac{c}{d}\sqrt{\tau_{d1}^2 + \tau_{d2}^2}\right)$. (3)

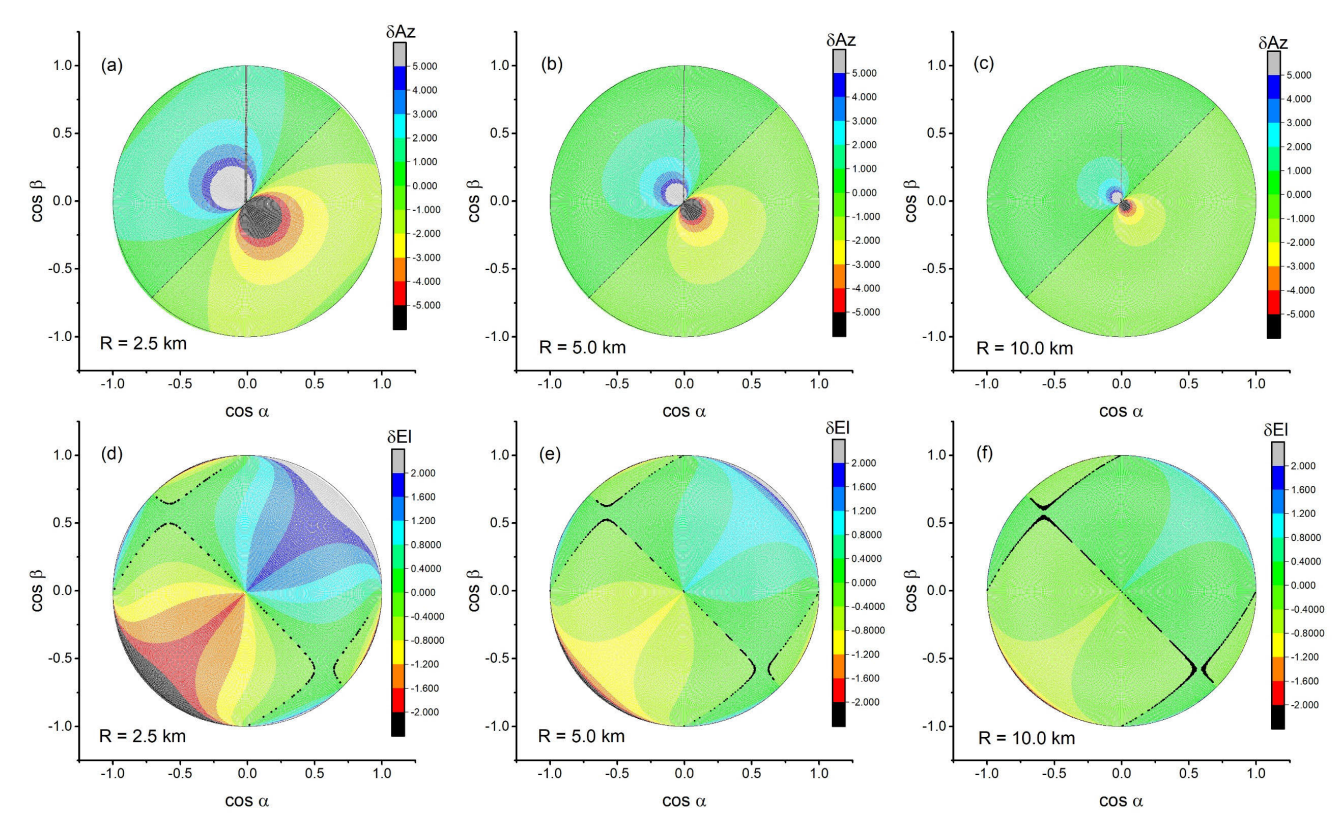


Fig. 2. (a)—(c) Azimuthal and (d)—(f) elevation errors for a 100-m orthogonal baseline configuration, projected onto the unit circle direction cosine plane, corresponding to the equatorial plane of a unit radius celestial hemisphere, for radial source distances of 2.5, 5, and 10 km. The baselines form a right triangle with the open side to the northeast. The elevation errors are symmetrical about 45° and 225° azimuth between the baselines and have antisymmetric maximal values along this axis, which corresponds to the perpendicular bisector of the triangle's hypotenuse. The azimuthal errors are the largest slightly off-vertical incidence along the perpendicular SE/NW axis.

For the more general case of multiple, nonorthogonal baselines, Stock [17] and Stock and Krehbiel [29] showed that the source location corresponds to the intersection of straight lines in the unit circle direction cosine projection space, with each line being perpendicular to its corresponding baseline and given by

$$\cos(\alpha)\sin(\theta_{ij}) + \cos(\beta)\cos(\theta_{ij}) = \frac{c\tau_{ij}}{d_{ij}}$$
(4)

where $\cos(\alpha)$ and $\cos(\beta)$ are the direction cosines, θ_{ij} is the angle between the baseline and due north, d_{ij} is the length of the baseline between antennas i and j, and τ_{ij} is the time difference signal arriving at antennas i and j. In general, the lines do not intersect at a common point, but accurate estimates of the 2-D coordinates $[\cos(\alpha), \cos(\beta)]$ of the radiation source can be obtained by solving (4) using standard least-squares techniques [17], [29], [30], [31], [32]. Once located in the cosine space, the corresponding 2-D azimuth and elevation angles are obtained by projecting the location up onto the unit celestial hemisphere, according to

$$Az = \arctan\left(\frac{\cos(\alpha)}{\cos(\beta)}\right)$$

$$El = \arccos\left(\frac{\cos(\beta)}{\cos(Az)}\right). \tag{5}$$

The above constitutes the basic principles of correlation-based short-baseline TDOA interferometry. With a multiplicity of baselines, the sources can be imaged by accumulating (adding) the correlation functions of the different baselines over the full cosine projection plane [17], [29], [25].

B. Determining the Systematic Error of the Plane Wave Model

The radiation signal emitted by lightning discharge processes, especially in the VHF band and with high time resolution of interferometer measurements, more closely resembles that of a localized point source than a broadly distributed source. Thus, the point spherical wave model in Fig. 1(b) (shown in 2-D for simplicity) better depicts the actual situation. Radiation originating at point O is transmitted to antennas A and B at the speed of light, with the transmission distances being $\|OA\|$ and $\|OB\|$. Instead of the path difference $c\tau_d$ between the two antennas corresponding to the perpendicular distance PA, as shown in Fig. 1(a), it corresponds to QA due to OQ and OB having the same length and forming an isosceles triangle with O.

The situation is shown in more detail in the exaggerated geometrical construction of Fig. 1(c), where the red line AO' and angle α' depict the mislocated source direction obtained from the plane wave model. As shown in Fig. 1(b), OQ and OB correspond to the spherical wavefront reaching antenna B. Also, as shown in Fig. 1(b), the observed length/time difference $c\tau_d$ corresponds to QA. When drawing a circle with $c\tau_d$ as the radius in Fig. 1(c), only one point P' can be found,

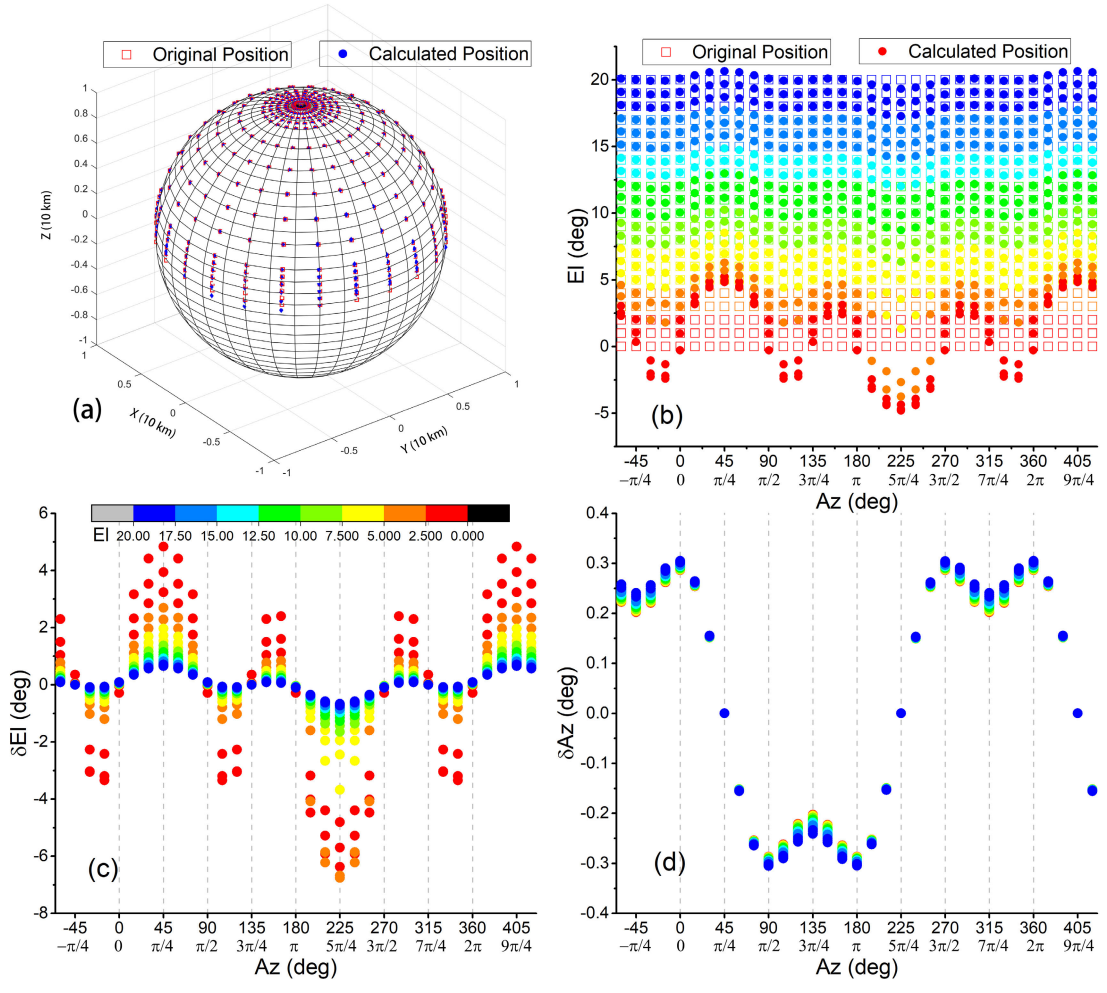


Fig. 3. Location errors of radiation sources below 20° elevation for the 100-m orthogonal baseline scheme at 10-km range. (b) and (c) Elevation error, showing the 45°/225° antisymmetric structure of the errors. (d) Azimuthal errors. In the orthogonal baseline observation scheme, the location errors of the radiation source with a low-elevation angle of incidence (lower than 20°) are at a distance of 10 km. (a) Simulation results displayed on a spherical surface at a distance of 10 km. (b) Azimuth-elevation view of the simulation results. (c) Elevation errors of the radiation signal incident at different azimuth angles. (d) Azimuth errors of the radiation signal incident at different azimuth angles. The colors in (b)–(d) represent the elevation angle, and the legend in each figure is the same as that in (c).

which makes $AP' \perp BP'$, which is at a higher angle α' that would be obtained from using the measured $c\tau_d$ value in the right triangle expression of (1).

The above construction illustrates the effect in 2-D with the coordinate origin being at antenna A. As will also be shown later, the elevation angle α appears to be higher when the source is in the upper right quadrant of the direction cosine space and lower when the source is in the lower left quadrant. In both cases, the effect is exaggerated for sources at low elevation angles, with sources at low elevation in the lower left quadrant appearing to be below the local horizon. The 2-D results of Fig. 1(c) are readily calculated numerically by a series of geometric constructions along the lines discussed above. The 3-D case is depicted geometrically in the following text and is more complex, with the systematic errors being more simply obtained from numerical simulation, as we discuss next.

C. Simulation Approach

The simulation computations are performed for two typically used and basic configurations of three antennas, namely,

orthogonal and equilateral triangle baseline, each with baseline lengths of 100 m. A grid in polar coordinates is adopted for the simulation: the azimuth angle is $0^{\circ} \sim 360^{\circ}$ and the elevation angle is $0^{\circ} \sim 90^{\circ}$, both with a grid spacing of 0.5° , and at distances ranging from 1 to 25 km, with a grid spacing of 500 m. For each 3-D grid point, the arrival times at the three antennas are analyzed with the plane wave formulations, and the results are compared both with the actual 2-D azimuth and elevation directions and in the direction cosine projection space. A total of 6.35 million radiation sources are simulated for each baseline layout, making it easy to visualize the deviations in the direction of cosine space. The analyses would be readily extended to any configuration and number of antennas.

III. SIMULATION RESULTS

A. Orthogonal Baselines

Orthogonal baseline layouts have been a common observation scheme in lightning interferometry [12], [16], [18], [28], [34], [35]. In the simulation, three antennas form two orthogonal baselines (AB and AC), with the length of baselines being 100 m, forming a right triangle in the first quadrant of

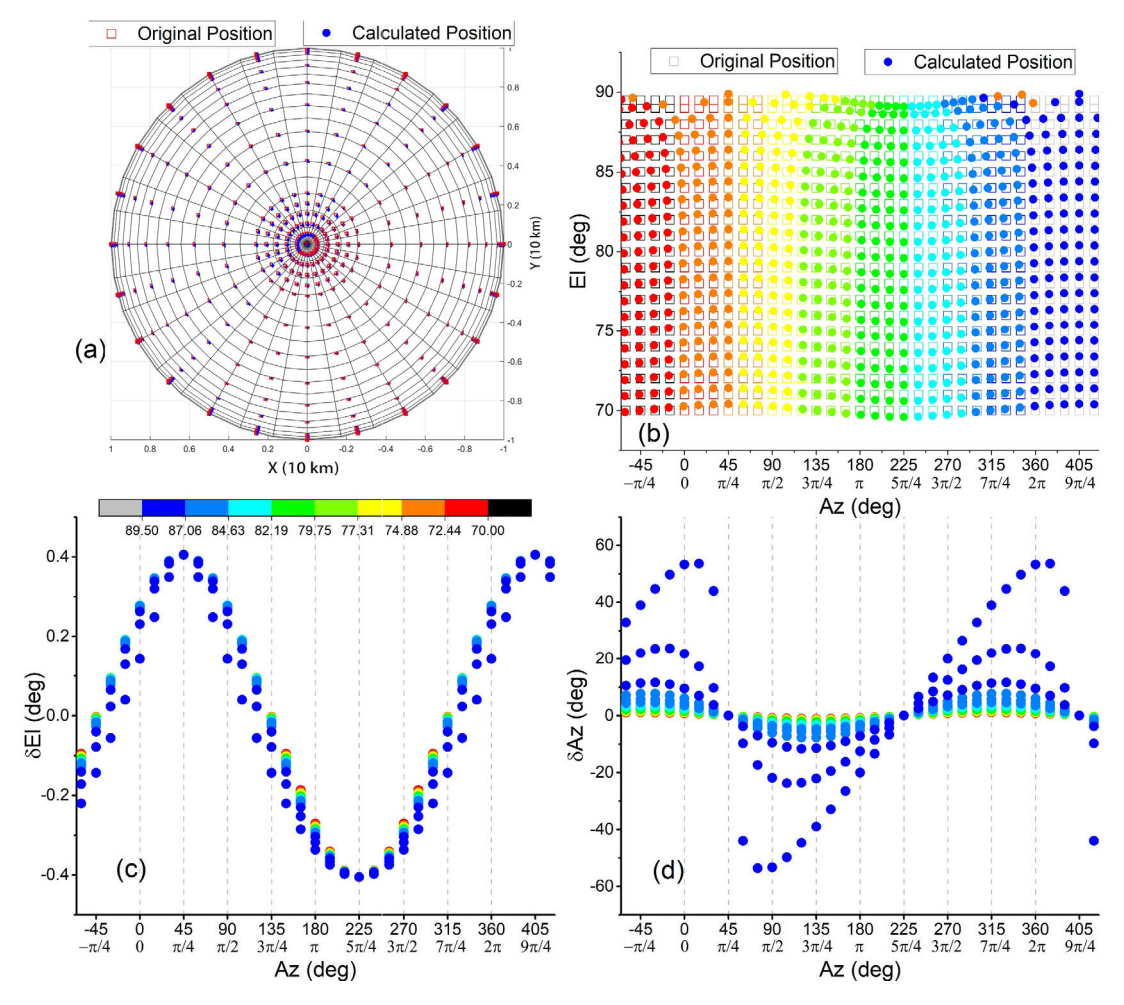


Fig. 4. In the orthogonal baseline observation scheme, the location error of the radiation source with a high-elevation angle of incidence ($El \ge 70^{\circ}$) at a distance of 10 km. (a) Spherical display of the simulation results at a distance of 10 km. (b) Azimuth-elevation view of the simulation results, where the color represents the azimuth. (c) Elevation error of radiation signals incident at different azimuth angles. (d) Azimuth error of radiation signals incident at different azimuth angles. The colors in (b)–(d) represent the elevation angle, and the legend in each figure is the same as that shown in (c).

the coordinate system. In accordance with the above studies, antenna A is used as the coordinate origin.

Fig. 2 shows the azimuth and elevation errors as viewed in the $[\cos(\alpha), \cos(\beta)]$ direction cosine plane of the measurements, corresponding to the equatorial plane of a unit radius celestial sphere [see Fig. 3(a)]. The results are shown for sources at radial distances of 2.5, 5, and 10 km from the origin, with the errors decreasing with increasing distance. As expected from the symmetry of a right triangle, both the azimuth and elevation errors are symmetric at about 45° and 225° azimuth (NE/SW diagonal), corresponding to the perpendicular bisector of the right triangle's hypotenuse. A somewhat weaker axis of symmetry occurs along the perpendicular NW/SE axis passing through antenna A.

To illustrate the symmetries, similar color tables are used for positive and negative errors, with positive errors greater than 5° bounded by light gray and negative errors by black. The transition between positive and negative errors is indicated by black dashed lines. Most striking is the elevation errors for close (2.5 km) sources shown in Fig. 2(d), which are increasingly positive to the NE and negative to the SW, with low elevation sources not reaching the horizon to the NE and appearing to

go below the horizon to the SW. Conversely, the azimuthal errors (top row) increase in magnitude toward the zenith, with the errors being positive to the NW and negative to the SE, with perfect symmetry about the main NE/SW axis. Before proceeding, we note that locations depicted as being below the horizon are imaginary rather than real values due to the measured values of $[\cos(\alpha), \cos(\beta)]$ lying outside the unit circle, causing $z = \operatorname{sqrt}\{1 - (x^2 + y^2)\}$ to be imaginary. The magnitude of the result is assigned to be a negative elevation angle.

Figs. 3 and 4 show the results in more detail, first within 20° elevation of the equatorial plane [see Fig. 3(b) and (c)] and second within 20° of the zenith, as viewed from above the polar axis [see Fig. 4(b) and (c)]. In both figures, the results are shown for sources at a 10-km slant range. Even for sources at this distance, from Fig. 3(b), it can be seen that a source at the horizon due NE (45° azimuth) appears to be at 5° elevation angle [lowest red dot in Fig. 3(b) and consistent with 5° positive elevation error in Fig. 3(c)]. Elevation errors as large as 3° extend over an azimuthal width of $\pm 30^{\circ}$ around the NE direction [see Figs. 2(f) and 3(c)]. Also, smaller, 2° positive elevation errors occur between 135° and 180° (SSE) and 270°–315° (WNW) azimuthal directions in

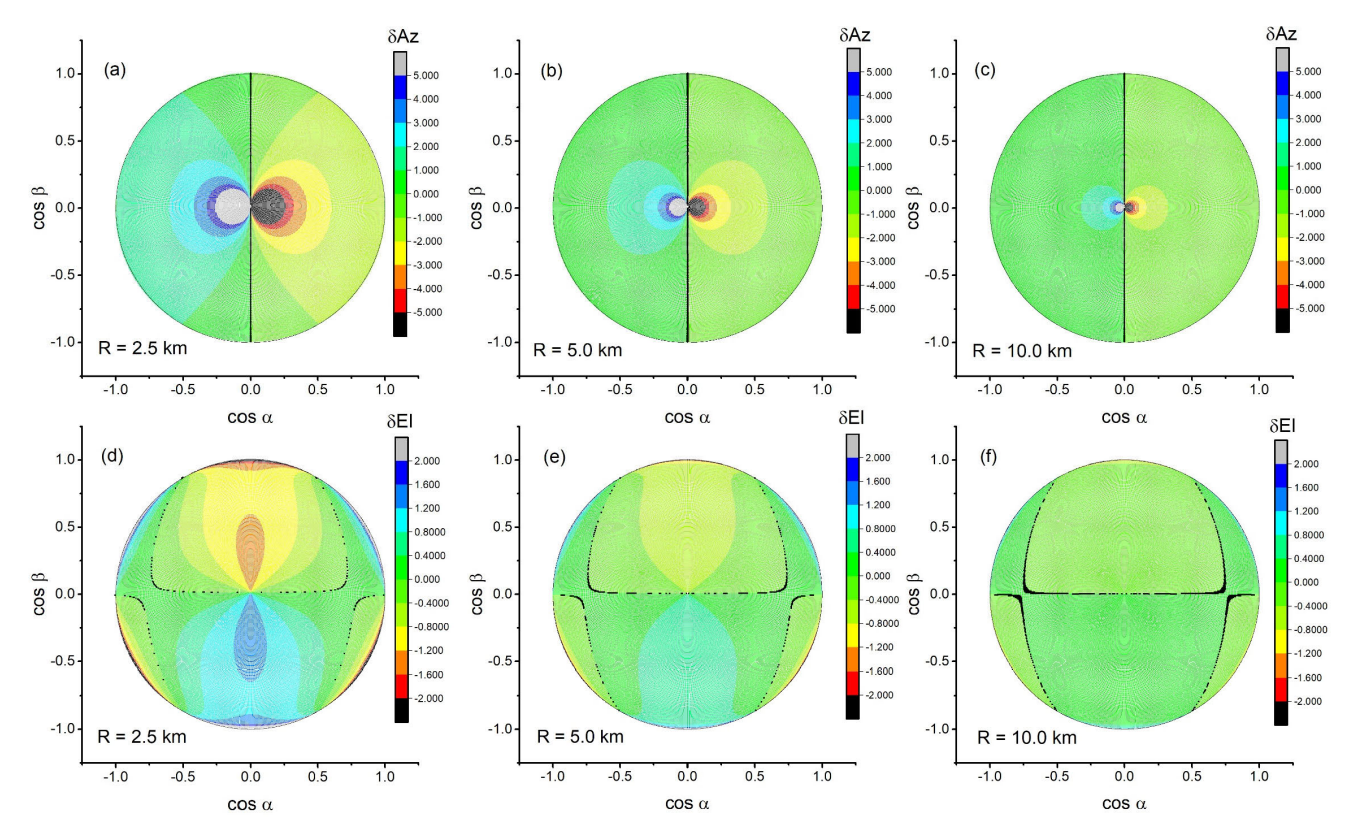


Fig. 5. Distributions of the location errors of the radiation source under an equilateral triangle baseline (the coordinate origin is at antenna A) at different distances projected onto the cosine plane. (a)–(c) Observation distances of 2.5, 5, and 10 km. (d)–(f) Corresponding elevation errors at the different observation distances.

Fig. 3(c), corresponding to extensions of the black \pm polarity boundary in those directions in Fig. 2(d)–(f). Conversely, sources at 5° elevation to the SW and 3° elevation separately to the ESE and NNW are artificially low in elevation (i.e., at or below the horizon), causing any activity at lower elevation angles, such as strokes to ground, to not be located in their final stage. At the 10-km range, this loss of sources below $+3^{\circ}$ and $+5^{\circ}$ elevation corresponds to $\sim 500-900$ -m altitude above ground level.

Conversely, the azimuthal errors at low elevation angles are relatively small [see Fig. 3(d)], passing through zero along the main NE/SW axis of symmetry and being between $+0.3^{\circ}$ and $+0.2^{\circ}$ to the north and west (\sim 50–35-m horizontal distance at the 10-km range) with analogous negative displacements to the east and south. The situation is reversed near the zenith (see Fig. 4), where the azimuthal errors are large [up to $\sim 50^{\circ}$ at 89° elevation and $\sim 20^{\circ}$ at 88° elevation; see Fig. 4(d)] but occur with decreasing radius, which, at 10-km altitude, corresponds to \sim 100–150-m azimuthal error within \sim 500-m distance from the pole. As can be seen from the upper part of Fig. 4(b), the azimuthal errors cause the sources to converge in azimuth as they approach the zenith from the SW and diverge away from each other in approaching the NE. As can be seen in Fig. 4(c), the elevation errors have a simple sinusoidal variation with azimuth, being positive to the NE and negative to the SW, as at low elevation angles, but smaller in magnitude.

Finally, at the lower range/altitudes of Fig. 2(a) and (b), the azimuthal errors became systematically larger to the point that

overhead sources are significantly mislocated rotationally by $\pm 5^{\circ}$ or so.

B. Equilateral Triangle Baselines

In recent years, the layout of interferometers has been gradually adjusted from an orthogonal baseline configuration to an equilateral or isosceles triangle baselines, as in studies [21], [24], [25], [26], [36], [37], [38]. Here, we simulate the three-antenna equilateral configuration operated at the Kennedy Space Center (KSC) in 2016 by Tilles et al. [24], [25], which had extended baseline lengths of 100 m, with the northernmost antenna, A, being used as the coordinate origin. As in Section III-B, Fig. 5 shows the elevation and azimuthal errors of the radiation source in the direction cosine projection plane for slant ranges R of 2.5-, 5-, and 10-km ranges. Figs. 6 and 7 show expanded views of the errors at low and overhead elevation angles, again for sources at the 10-km slant range. For this spatiotemporal configuration, the main axis of symmetry is in the north-south direction passing through antenna A. Due to there being only one axis of symmetry, the errors in the direction cosine planes of Fig. 5 are similar to those of the orthogonal baseline results of Fig. 2, except for being rotated 45° CCW and flipped N-S-wise, and being somewhat weaker.

The similarity with the orthogonal baseline results is due to the orthogonal system also being triangular, with the coordinate origin located at the apex of the triangle. In particular, a similarly rotated and N-S flipped orthogonal

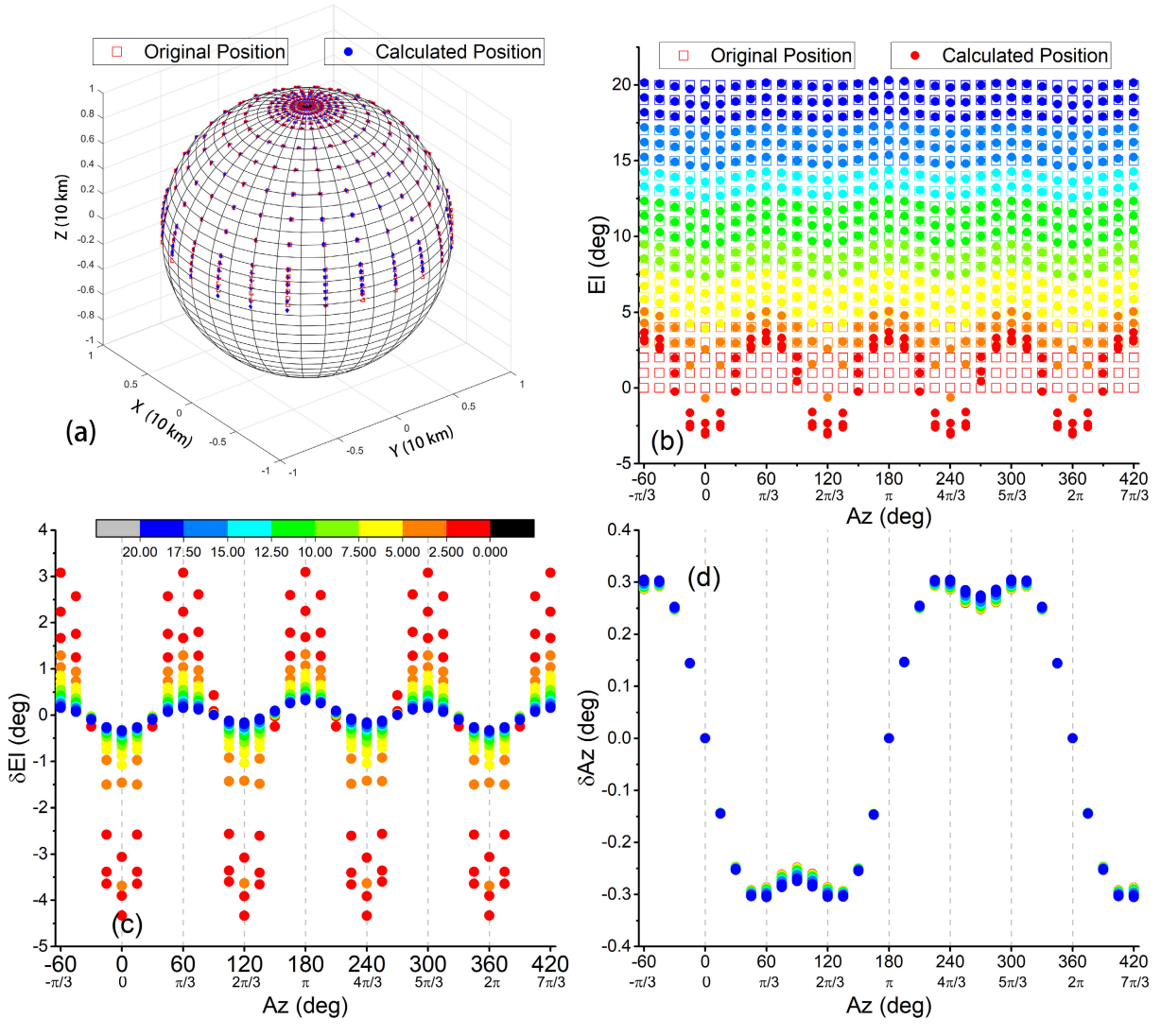


Fig. 6. In the equilateral triangle baseline scheme (the coordinate origin is at antenna A), the location errors of the radiation source with a low-elevation angle of incidence (El $< 20^{\circ}$) at a distance of 10 km. (a) Display of the simulation results at a distance of 10 km on a spherical surface. (b) Azimuth-elevation view of the simulation results. (c) Elevation errors of the radiation signal incident at different azimuth angles. (d) Azimuth errors of the radiation signal incident at different azimuth angles. The colors in (b)–(d) represent the elevation angle, and the legend in each figure is the same as that in (c).

configuration constitutes a right isosceles triangle, with the coordinate origin being at the northern apex of the triangle in both cases. The east—west baseline at the bottom of the rotated orthogonal system would be longer than for the equilateral configuration, providing improved angular resolution for the elevation measurements in the E-W direction, but less angular resolution and increased elevation errors in the N-S direction. A similar shortening of the effective N-S extent occurs for the equilateral configuration but by a lesser amount, causing the elevation errors to be weaker for the equilateral than for the orthogonal case [compare Figs. 2(d) and 5(d)].

In both cases, the apparent below-horizon negative errors occur in the direction away from the apex and coordinate origin, in this case northward, and the positive elevation errors occur southward, in the direction of the perpendicular bisector of the opposite baseline. Similar to the orthogonal baseline results, the elevation plots of Fig. 5 exhibit additional errors at alternating sets of three different low elevation angles,

associated with the triaxial symmetries of the equilateral configuration. The errors are seen in greater detail in Fig. 6(c) that shows the elevation errors in greater detail. In particular, negative elevation errors occur at azimuths of 0°, 120°, and 240°, and positive errors occur at 180°, 300°, and 60°, as having perfect triaxial symmetry. Along each axis, and similar to the orthogonal case, positive elevation errors occur on the perpendicular bisector of the corresponding baseline, and negative errors occur on the oppositely located apex of the triangle. Instead of the positive error having a peak value of 5°, as in the orthogonal case, the maximum error and lowest locatable elevation angle is 3° [lowest red dot at 60°, 180°, and 300° in Fig. 6(b)]. Otherwise, the elevation observations have a perfect $2\pi/3$ or 120° periodicity. Surprisingly, the azimuthal error at the low elevation angle [see Fig. 6(d)] does not have the triaxial symmetry but is related to the main N-S axis of symmetry, analogous to the azimuthal errors of the orthogonal system. As will be shown in Section III-C, this is entirely due

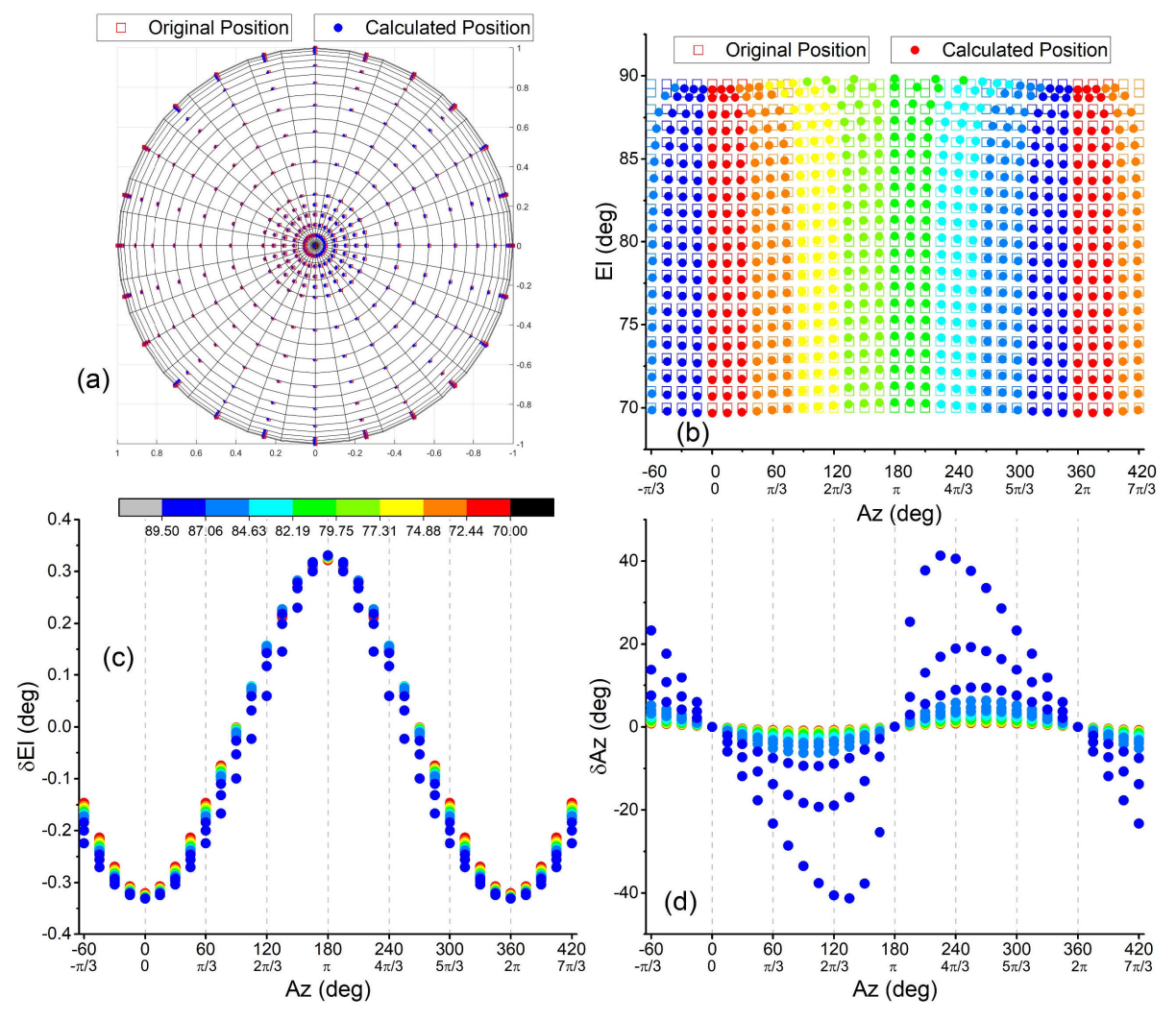


Fig. 7. In the case of the equilateral triangle baseline (the coordinate origin is at antenna A), the location errors of the radiation source with a high-elevation angle of incidence ($EI > 20^{\circ}$) at a distance of 10 km. (a) Display of the simulation results at a distance of 10 km on a spherical surface. (b) Azimuth-elevation view of the simulation results, where the color represents the azimuth. (c) Elevation errors of the radiation signal incident at different azimuth angles. (d) Azimuth errors of the radiation signal incident at different azimuth angles. The colors in (b)–(d) represent the elevation angle, and the legend in each figure is the same as that in (c).

to the coordinate system being located asymmetrically, at one of the apexes of the triangle.

Finally, Fig. 7 shows the elevation and azimuthal errors at high elevation angles around the zenith. Consistent with the azimuthal errors not differing in nature from those of the orthogonal configuration and being related to the main axis of symmetry, the error plots of Fig. 7 are similar to the orthogonal results, except for being shifted by 45° in azimuth and having slightly smaller error values. For the equilateral case, the apparent sources are displaced negatively or northward on the east side of the zenith and positive but also northward on the west side by up to 40° azimuth [see Fig. 7(d)]. Similarly, the elevation angles are displaced positively or northward on the south side of the zenith, and negatively and also northward on the north side [see Fig. 7(c)], with the net effect being a northward error around the zenith, also an effect of the coordinate origin being located asymmetrically. While triaxial symmetries are seen in the elevation plots at

low elevation angles, they are not seen in the azimuthal plots at high elevation angles.

C. Fully Symmetric Equilateral Configuration

Although the configuration described above makes use of equilateral spatial symmetry to optimize the elevation errors at low elevation angles, from an overall standpoint, the errors remain similar to those produced by an orthogonal network. In this section, we show that this results from the coordinate origin being asymmetrically located at one of the antenna locations. Although the initial equilateral configuration is axisymmetric, it is not centrosymmetric. By locating the coordinate origin at the center of the equilateral triangle, full advantage can be taken of the equilateral symmetry [32].

Fig. 8 shows the results of having the coordinate origin centrally located. Instead of having only one axis of symmetry, as before, the results have full triaxial symmetry. To show the results more clearly, the color tables are changed to

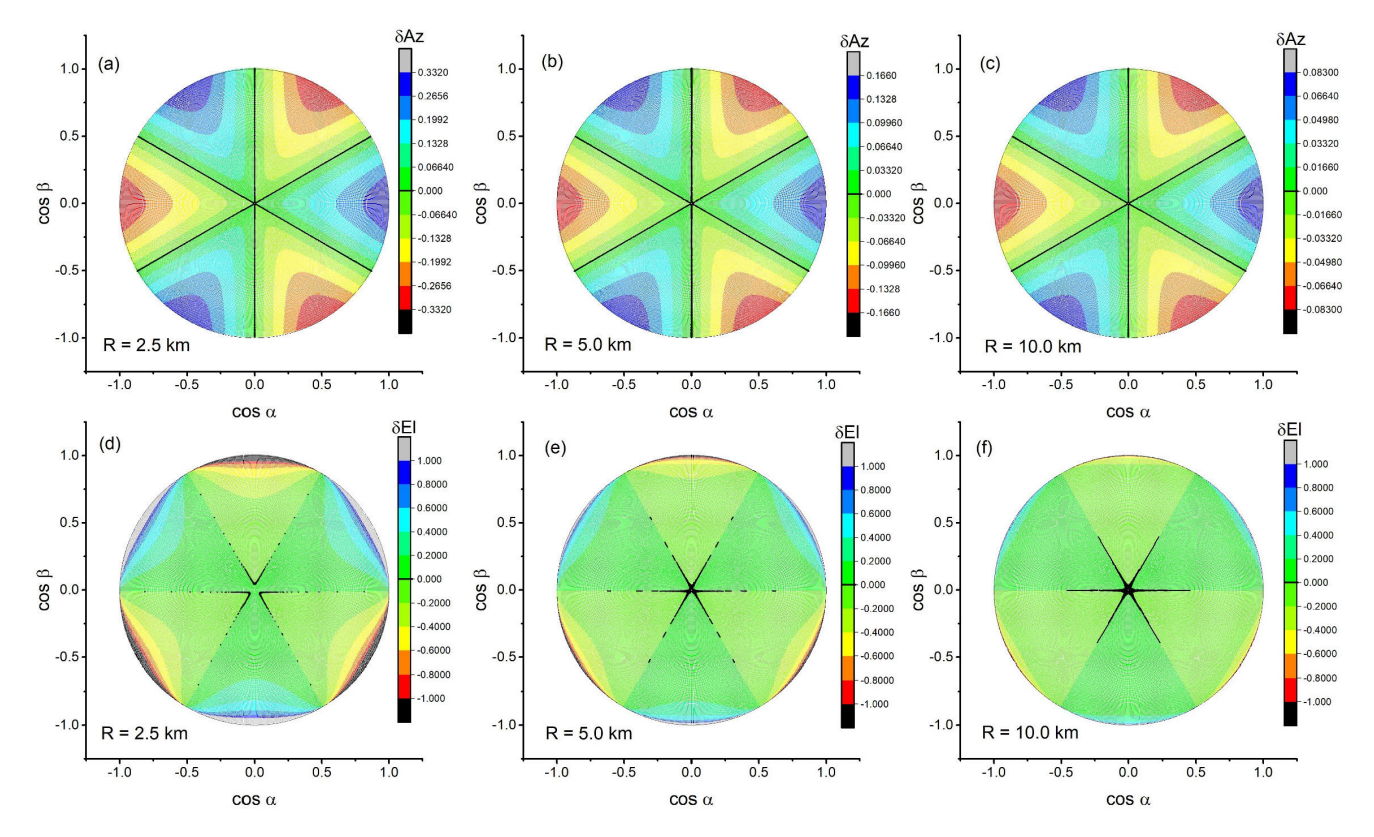


Fig. 8. Distributions of the location error of the radiation source at different distances on the cosine projection plane in the case of an equilateral triangle baseline [the coordinate origin is at the center of the triangle. (a)–(c) Azimuth error corresponding to observation distances of 2.5, 5, and 10 km. (d)–(f) Corresponding elevation errors.

differentiate between positive and negative errors, and the scales are made more sensitive to the reduced error values. For the elevation plots, the errors span the range $\pm 1^{\circ}$ (versus $\pm 2^{\circ}$ in Figs. 2 and 5). For the azimuthal plots of Fig. 8(a)–(c), the color tables for the different slant ranges are individually scaled to match the maximum values around the edge of the unit circles. In particular, for sources in the 2.5-km range, the maximum azimuthal error at 0° elevation is $\pm 0.332^{\circ}$, corresponding to a spatial displacement of ± 15 m due to the waveform sphericity. At 5- and 10-km ranges, the maximum errors are reduced by factors of 2 and 4, respectively, to $\pm 0.166^{\circ}$ and 0.083° so that the 15-m maximum spatial displacement is independent of range. At higher elevation angles, the spatial displacements are successively smaller, to the point of being zero at the zenith, and, thus, are not shown. Sources directly overhead of the array center will arrive at the same time at each of the antennas. The azimuthal errors in the vicinity of the zenith for the other configurations are, therefore, the result of having an asymmetric coordinate origin.

Fig. 9 shows the errors at low elevation angles in more detail. As for the previous equilateral configuration, the elevation results continue to have perfect triaxial symmetry, owing to the low-altitude angles being unaffected by and independent of the coordinate origin. The positive errors have maximum values of $\sim 3^{\circ}$ in perpendicular baseline directions, consistent with and indicating strokes to ground appearing to terminate 3° above the horizon in these directions [see Fig. 9(b)]. In the supplemental directions away from the equilateral vertices,

the sources have negative errors and appear to go below the horizon.

On the other hand, and as seen in the upper figures of Fig. 8, the low-altitude azimuthal values are completely different from those of the other two configurations. The difference is also seen in the quantitative error values of Fig. 9(d). For the asymmetric equilateral and orthogonal cases, the azimuthal errors are dominated by the unidirectional symmetry associated with the coordinate origin, being positive on one side of the axis and negative on the other side [see Figs. 3(d) and 6(d)]. In addition, the values were approximately constant on the two sides, at $\sim \pm 0.3^{\circ}$. With the symmetric coordinate origin, the errors have the same kind of triaxial symmetry as the elevation errors and are more sinusoidal in nature. At the same time, the maximum values are reduced to $\pm 0.08^{\circ}$, making them largely insignificant.

IV. DISCUSSION

VHF interferometer observations of lightning typically assume the incident radiation to be a plane wave because the antenna baselines are relatively short (~ 100 m). However, for localized sources at close distances or with longer baselines, neglecting the spherical nature of the wavefront can produce noticeable errors in the 2-D arrival direction that affects a comparison of the radiation sources with other observations, such as dual interferometer measurements for obtaining 3-D observations. The errors can be significant even for sources at distances of 5–10 km or more. In addition, the plane

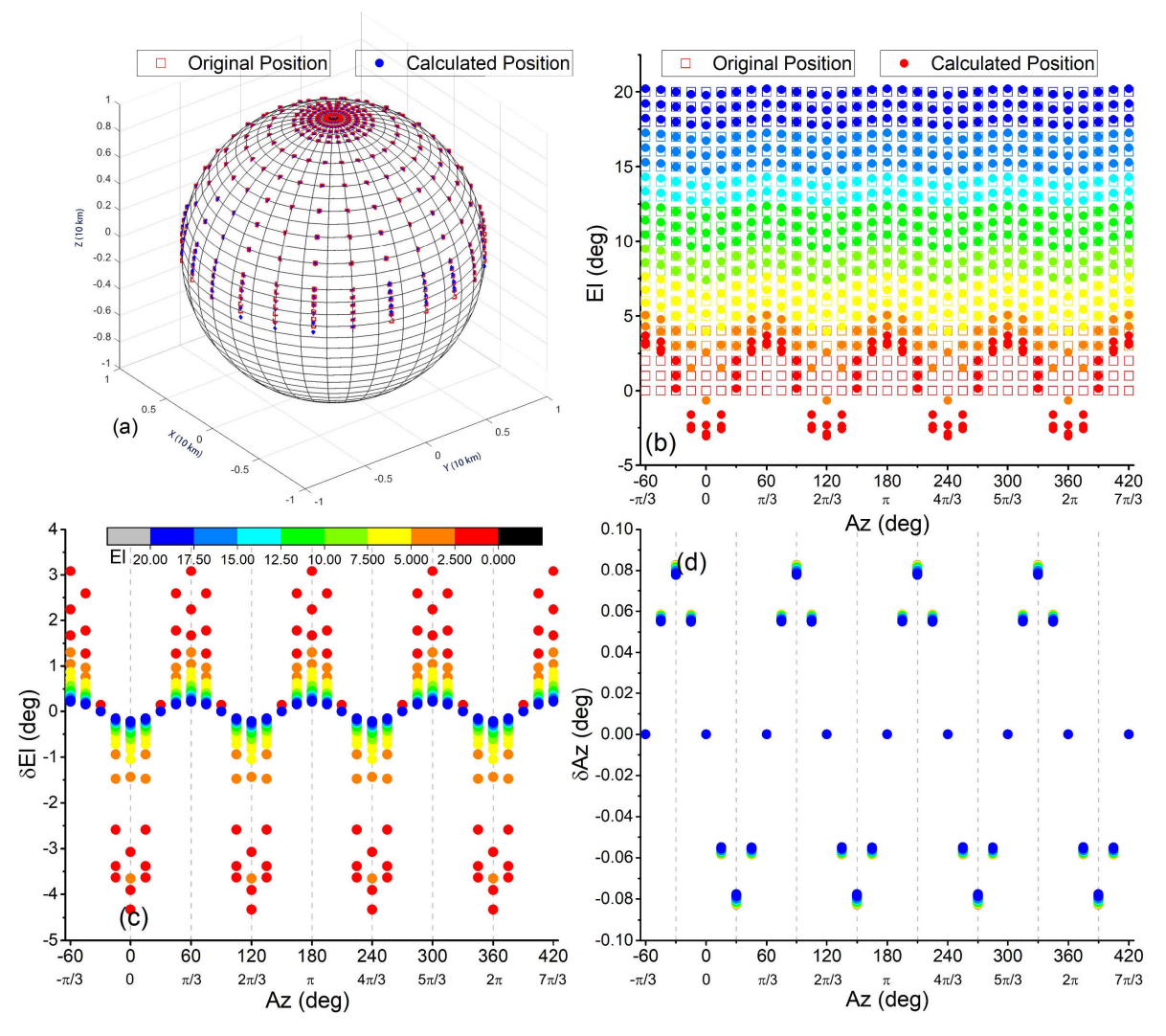


Fig. 9. Location errors of the radiation source incident at a low elevation angle (E (E (E)) at a distance of 10 km in the equilateral triangle baseline observation scheme (the coordinate origin is in the center of the triangle). (a) Display of the simulation results at a distance of 10 km on a spherical surface. (b) Azimuth-elevation view of the simulation results. (c) Elevation errors of the radiation signal incident at different azimuth angles. (d) Azimuth errors of the radiation signal incident at different azimuth angles.

wave assumption is totally inappropriate when using a larger number of antennas with expanded baselines to obtain 3-D observations from a single interferometer system.

As shown in this article, systematic errors can be minimized by utilizing increasingly symmetrical triangular antenna arrangements and choice of coordinate origin, with the optimum configuration being an equilateral triangle with the coordinate origin at the center of the triangle. It is not surprising that increasing the symmetry of the antenna configuration reduces systematic errors, as symmetry is a powerful mathematical tool in investigating and understanding nature.

A. Geometric Explanation of Elevation Errors

Fig. 10 shows the basic geometry of how the plane wave assumption produces elevation errors. For simplicity, this is done for the orthogonal antenna configuration, utilizing a rotated coordinate frame along the 45° axis of symmetry, which is where the largest elevation errors occur. The basic approach applies to the equilateral cases as well. The geometric construction shows that the errors are due to an

unavoidable left/right asymmetry of triangular configurations, whereby sources on the right-hand side (open angle) of the triangle have shorter 3-D propagation distances to the laterally positioned (B and C) antennas than on the left-hand side (closed angle) of the triangle [see Fig. 10(a)].

Focusing on the right-hand side in Fig. 10(a) and (b), the spherical wavefront from a source at "O" arrives simultaneously at antennas B and C, with spherical radii $R_C = R_B$, corresponding to the 3-D slant range between O and B, C. Numerically, for a source O at x, y, z = [10, 0, 5] (arbitrary units, as used in the figure) and for C = [3, 3, 0] and B = [3, -3, 0], $R_{B,C} = \operatorname{sqrt}(7^2 + 5^2 + 3^2) = 9.11$ units, while $R_A = \operatorname{sqrt}(10^2 + 5^2) = 11.18$ units, corresponding to the radii of the spherical wavefront at the two points in time/distance. The incident angle at A is $\alpha = \tan^{-1}(5/10) = 26.6^\circ$, and the propagation difference of arrival is $\Delta R = R_A - R_{B,C} = 2.07$ units. The question is at what incidence angle α' would a plane wave need to have that produces the same propagation difference ΔR between arriving at B, C [i.e., point D in Fig. 10(b)] and arriving at A.

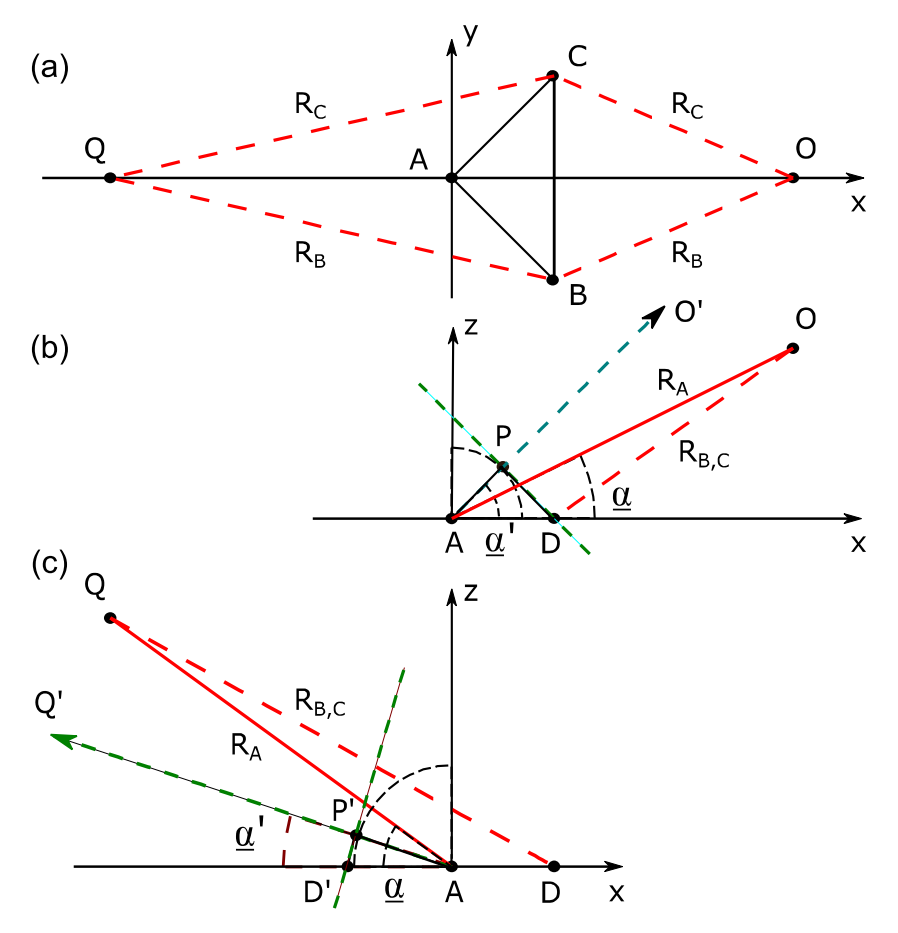


Fig. 10. Geometric model for elevation errors along the axis of symmetry for an orthogonal antenna configuration. The red lines correspond to the actual source propagation distances, with the dashed lines indicating a 3-D component into and out of the page. The dashed green line passing through PD in (b) corresponds to the plane wave that would have the same propagation difference of arrival as the spherical wave of the source at O, which has an apparent incidence angle α that is always greater than the actual angle α . (a) Two typical examples (O, Q) under orthogonal baselines; (c) corresponds to the plane wave that would have the same propagation difference of arrival as the spherical wave of the source at Q, which has an apparent incidence angle α' that is always smaller than the actual angle α .

Geometrically, the answer is obtained by drawing a circular arc around A of radius $\Delta R = 2.07$ units and drawing a line through point D to a point of tangency P with the arc, at which point the additional propagation distance to A will be $\Delta R = \mathrm{AP}$ in Fig. 10(b). The dashed line passing through points D and P corresponds to the plane wave upon reaching antennas B and C, and the perpendicular line from A through P indicates the plane wave-determined apparent direction α' of the source at an undetermined distance O'. As can be seen from the construction, the apparent elevation angle α' is larger than the incident angle α , constituting a positive error in the source direction.

Quantitatively, α' can be determined by noting that APD in Fig. 10 constitutes a right triangle, for which $\cos(\alpha') = \Delta R/AD = 2.07/3$ or $\alpha' = 46.4^{\circ}$, considerably larger than the actual α .

As noted above, the error is increased by antennas B and C being laterally displaced from the x-axis of symmetry. This increases the radius of curvature over what would be obtained by an equilateral or laterally narrower isosceles configuration, which, in turn, decreases the propagation difference ΔR and central radius AP, tilting the incidence angle to increasingly higher elevation angles and positive systematic error.

For sources on the opposite end of the axis of symmetry, the situation is reversed, namely, the elevation angle of sources is lower rather than higher [see Fig. 10(c)]. The basic reason for this is that antennas B and C are further away from A, rather than closer, so that $R_{\rm B,C}$ is greater than $R_{\rm A}$.

B. Optimization Scheme

Through the above location simulation and analysis of interferometers in an orthogonal baseline layout and an equilateral triangle baseline layout, the location results under the latter are intuitively better than those under the former regardless of the viewing angle, and the advantages are obvious under some conditions. From the analysis of the distribution characteristics of the location errors of the interferometers under the two baseline configurations, the symmetry of the interferometer antenna layout is clearly a highly important factor affecting the location results. Naturally, enhancing the symmetry of the interferometer antenna layout should effectively optimize the systematic error of the interferometric location system.

In terms of plane geometry, the symmetry of geometric figures includes axial symmetry and central symmetry. The equilateral triangle interferometer layout has three axes of

symmetry, while the orthogonal baseline interferometer layout has only one. The analysis of the systematic error model in Fig. 1(c) indicates that this difference is indeed one of the reasons why the orthogonal baseline interferometer layout has a more significant systematic error. The above baseline layouts take an antenna as the coordinate origin, and there is no centrosymmetry, which leads to the 2π oscillation error in the azimuth. The equilateral right triangle does not have a central point of symmetry, while the equilateral triangle has a center of symmetry, which fully conforms to the above analytical idea of optimizing the systematic error. In addition, simulations and analysis show that avoiding perpendicular baselines formed by pairs of antennas can significantly suppress the occurrence of systematic errors in the system. In summary, the optimal antenna layout scheme should have the following features: 1) multiple antennas forming an axis-symmetric distribution; 2) central symmetry; and 3) avoiding perpendicular baselines. However, considering that the more antennas there are, the more difficult it is to synchronize data acquisition; the greater the computational burden on the positioning algorithm, the number of antennas in the interferometer system cannot be increased indefinitely.

Therefore, based on the research in this article, we propose an observation scheme for an interferometer composed of five VHF antennas. These five antennas form a regular pentagon that satisfies the requirements of axis symmetry, central symmetry, and no perpendicular baselines. Of course, the minimum configuration that can simultaneously satisfy these conditions is when there are five antennas. For this layout scheme, we also conducted a simulation analysis of systematic errors similar to other schemes. As expected, the simulation results perfectly eliminated the systematic errors caused by the plane wave approximation. Since the systematic errors can indeed be eliminated using this observation scheme, we cannot show its effect with images like other schemes shown in this article. This optimized interferometer layout scheme has been applied in our Utah lightning and terrestrial gamma-ray flash (TGFs') observation, and we will present and analyze the new results in another paper.

V. CONCLUSION

The interferometer measurement of VHF RF signals emitted by lightning is a valuable technique for studying the lightning breakdown process. However, the assumption of RF signals propagating as plane waves in the traditional interferometric model introduces systematic errors in lightning location. This article proposes a conceptual model for the systematic error caused by the plane wave approximation and suggests that the baseline layout significantly influences the location error. Through simulations, it is confirmed that an equilateral triangle baseline layout outperforms the commonly used orthogonal baseline layout. Leveraging the symmetry of the equilateral triangle layout, the systematic error can be optimized using geometric relationships. The study proposes a baseline layout scheme with the center of an equilateral triangle as the coordinate origin, resulting in improved location accuracy. The azimuth error is minimized, and the azimuth and elevation errors exhibit periodic fluctuations with the incident azimuth

of the radiation source. Based on this study, we further propose the application of a highly symmetrical (axial and central symmetry) pentagonal (composed of five antennas) interferometer observation scheme for practical observations. Simulation results indicate that under this scheme, the systematic error caused by the plane wave approximation can be perfectly eliminated. The baseline length does not affect the distribution characteristics of the location error, and drawing distribution charts of the location error helps analyze the error levels. The proposed layout scheme enhances reliability in lightning observation, providing valuable insights for analyzing specific physical processes and performing reliability analyses of interferometric location results.

This work represents a significant contribution to the field of lightning observation using interferometric techniques. By identifying the systematic error caused by the plane wave model approximation and proposing an improved baseline layout scheme, we have addressed a crucial aspect of lightning research. Our simulations and analysis have demonstrated the superiority of the equilateral triangle baseline layout in reducing location errors and optimizing interferometric positioning.

Furthermore, our study sheds light on the importance of leveraging the symmetry of the baseline layout to improve the accuracy of interferometric location. We have highlighted the limitations of the traditional orthogonal baseline layout and provided a novel approach that makes full use of the symmetrical structure of not only the equilateral triangle but also the regular pentagon. This innovation significantly enhances the reliability and precision of lightning observations.

However, it is important to acknowledge that there are still some challenges to overcome. The elevation error associated with low-elevation angle incidents requires further investigation and potential mitigation strategies. In addition, the impact of different baseline lengths on location error distribution could be explored in future studies.

In conclusion, this work represents a valuable contribution to the field, providing new insights and approaches to improve the accuracy of interferometric lightning observations. We believe that our findings and proposed baseline layout scheme have the potential to inspire further research and advancements in this area, ultimately driving innovation and advancements in lightning studies.

ACKNOWLEDGMENT

The authors would like to thank the editors and anonymous reviewers for their constructive comments and suggestions, which greatly helped to improve the technical quality and presentation of this article.

REFERENCES

- J. W. Warwick, C. O. Hayenga, and J. W. Brosnahan, "Interferometric directions of lightning sources at 34 MHz," *J. Geophys. Res., Oceans*, vol. 84, no. C5, pp. 2457–2468, May 1979, doi: 10.1029/jc084ic05p02457.
- [2] C. O. Hayenga, "Characteristics of lightning VHF radiation near the time of return strokes," *J. Geophys. Res.*, Atmos., vol. 89, no. D1, pp. 1403–1410, Feb. 1984, doi: 10.1029/jd089jd01p01403.
- [3] P. Richard, A. Delannoy, G. Labaune, and P. Laroche, "Results of spatial and temporal characterization of the VHF-UHF radiation of lightning," *J. Geophys. Res., Atmos.*, vol. 91, no. D1, pp. 1248–1260, Jan. 1986, doi: 10.1029/jd091id01p01248.

- [4] C. T. Rhodes, "Interferometric observations of VHF radiation from lightning," Ph.D. thesis, Dept. Phys., New Mexico Tech., Socorro, NM, USA 1989
- [5] C. T. Rhodes, X. M. Shao, P. R. Krehbiel, R. J. Thomas, and C. O. Hayenga, "Observations of lightning phenomena using radio interferometry," *J. Geophys. Res., Atmos.*, vol. 99, no. D6, pp. 13059–13082, Jun. 1994, doi: 10.1029/94jd00318.
- [6] X. M. Shao, "The development and structure of lightning discharges observed by radio interferometer," Ph.D. thesis, Dept. Phys., New Mexico Tech., Socorro, NM, USA, 1993.
- [7] X. M. Shao, P. R. Krehbiel, R. J. Thomas, and W. Rison, "Radio interferometric observations of cloud-to-ground lightning phenomena in Florida," *J. Geophys. Res.*, Atmos., vol. 100, no. D2, pp. 2749–2783, Feb. 1995, doi: 10.1029/94jd01943.
- [8] X. M. Shao and P. R. Krehbiel, "The spatial and temporal development of intracloud lightning," J. Geophys. Res., Atmos., vol. 101, no. D21, pp. 26641–26668, Nov. 1996, doi: 10.1029/96jd01803.
- [9] G. Zhang, Y. Zhao, X. Qie, T. Zhang, Y. Wang, and C. Chen, "Observation and study on the whole process of cloud-to-ground lightning using narrowband radio interferometer," *Sci. China D, Earth Sci.*, vol. 51, no. 5, pp. 694–708, May 2008, doi: 10.1007/s11430-008-0049-9.
- [10] X. M. Shao, D. N. Holden, and C. T. Rhodes, "Broad band radio interferometry for lightning observations," *Geophys. Res. Lett.*, vol. 23, no. 15, pp. 1917–1920, Jul. 1996, doi: 10.1029/96gl00474.
- [11] Z. Kawasaki, R. Mardiana, and T. Ushio, "Broadband and narrowband RF interferometers for lightning observations," *Geophys. Res. Lett.*, vol. 27, no. 19, pp. 3189–3192, Oct. 2000, doi: 10.1029/1999gl011058.
- [12] R. Mardiana and Z. Kawasaki, "Broadband radio interferometer utilizing a sequential triggering technique for locating fast-moving electromagnetic sources emitted from lightning," *IEEE Trans. Instrum. Meas.*, vol. 49, no. 2, pp. 376–381, Apr. 2000, doi: 10.1109/19.843081.
- [13] S. Qiu, B. Zhou, L. Shi, W. Dong, Y. Zhang, and T. Gao, "An improved method for broadband interferometric lightning location using wavelet transforms," *J. Geophys. Res.*, Atmos., vol. 114, no. D18, pp. 1–9, Sep. 2009, doi: 10.1029/2008jd011655.
- [14] M. Akita et al., "What occurs in K process of cloud flashes?" J. Geophys. Res., Atmos., vol. 115, no. D7, pp. 1–7, Apr. 2010, doi: 10.1029/2009jd012016.
- [15] W. Dong, X. Liu, Y. Yu, and Y. Zhang, "Broadband interferometer observations of a triggered lightning," *Chin. Sci. Bull.*, vol. 46, no. 18, pp. 1561–1565, Sep. 2001, doi: 10.1007/bf02900582.
- [16] M. G. Stock et al., "Continuous broadband digital interferometry of lightning using a generalized cross-correlation algorithm," *J. Geo*phys. Res., Atmos., vol. 119, no. 6, pp. 3134–3165, Mar. 2014, doi: 10.1002/2013jd020217.
- [17] M. A. Stock, "Broadband interferometry of lightning," Ph.D. thesis, New Mexico Inst. Mining Technol., Socorro, NM, USA, 2014.
- [18] Z. Sun, X. Qie, M. Liu, D. Cao, and D. Wang, "Lightning VHF radiation location system based on short-baseline TDOA technique—Validation in rocket-triggered lightning," *Atmos. Res.*, vols. 129–130, pp. 58–66, Jul. 2013, doi: 10.1016/j.atmosres.2012.11.010.
- [19] W. Rison et al., "Observations of narrow bipolar events reveal how lightning is initiated in thunderstorms," *Nature Commun.*, vol. 7, no. 1, p. 10721, Feb. 2016, doi: 10.1038/ncomms10721.
- [20] M. G. Stock, P. R. Krehbiel, J. Lapierre, T. Wu, M. A. Stanley, and H. E. Edens, "Fast positive breakdown in lightning," *J. Geophys. Res.*, Atmos., vol. 122, no. 15, pp. 8135–8152, Aug. 2017, doi: 10.1002/2016jd025909.
- [21] Y. Zhang et al., "Observations of the initial stage of a rocket-and-wire-triggered lightning discharge," *Geophys. Res. Lett.*, vol. 44, no. 9, pp. 4332–4340, May 2017, doi: 10.1002/2017gl072843.
- [22] F. Lyu, S. A. Cummer, Z. Qin, and M. Chen, "Lightning initiation processes imaged with very high frequency broadband interferometry," *J. Geophys. Res.*, Atmos., vol. 124, no. 6, pp. 2994–3004, Mar. 2019, doi: 10.1029/2018jd029817.
- [23] Y. Pu and S. A. Cummer, "Needles and lightning leader dynamics imaged with 100–200 MHz broadband VHF interferometry," *Geophys. Res. Lett.*, vol. 46, no. 22, pp. 13556–13563, Nov. 2019, doi: 10.1029/2019g1085635.
- [24] J. N. Tilles et al., "Fast negative breakdown in thunderstorms," *Nature Commun.*, vol. 10, no. 1, p. 1648, Apr. 2019, doi: 10.1038/s41467-019-09621-z.
- [25] J. N. Tilles et al., "Radio interferometer observations of an energetic in-cloud pulse reveal large currents generated by relativistic discharges," J. Geophys. Res., Atmos., vol. 125, no. 20, Oct. 2020, Art. no. e2020JD032603, doi: 10.1029/2020jd032603.

- [26] J. W. Belz et al., "Observations of the origin of downward terrestrial gamma-ray flashes," J. Geophys. Res., Atmos., vol. 125, no. 23, Dec. 2020, Art. no. e2019JD031940, doi: 10.1029/2019JD031940.
- [27] G. C. Carter, "Coherence and time delay estimation," Proc. IEEE, vol. 75, no. 2, pp. 236–255, Feb. 1987, doi: 10.1109/PROC.1987. 13723
- [28] X. Shao, C. Ho, G. Bowers, W. Blaine, and B. Dingus, "Lightning interferometry uncertainty, beam steering interferometry, and evidence of lightning being ignited by a cosmic ray shower," *J. Geophys. Res.*, Atmos., vol. 125, no. 19, Oct. 2020, Art. no. e2019JD032273, doi: 10.1029/2019jd032273.
- [29] M. Stock and P. Krehbiel, "Multiple baseline lightning interferometry—Improving the detection of low amplitude VHF sources," in *Proc. Int. Conf. Lightning Protection (ICLP)*, Oct. 2014, pp. 293–300.
- [30] R. J. Thomas et al., "Accuracy of the lightning mapping array," J. Geophys. Res., Atmos., vol. 109, no. D14, Jul. 2004, Art. no. D14207, doi: 10.1029/2004jd004549.
- [31] X. P. Fan et al., "A new method of three-dimensional location for low-frequency electric field detection array," *J. Geophys. Res., Atmos.*, vol. 123, no. 16, pp. 8792–8812, Aug. 2018, doi: 10.1029/2017jd028249.
- [32] X. Fan et al., "Application of ensemble empirical mode decomposition in low-frequency lightning electric field signal analysis and lightning location," *IEEE Trans. Geosci. Remote Sens.*, vol. 59, no. 1, pp. 86–100, Jan. 2021, doi: 10.1109/tgrs.2020.2991724.
- [33] D. Jensen, R. G. Sonnenfeld, M. A. Stanley, H. E. Edens, C. L. da Silva, and P. R. Krehbiel, "Dart-leader and K-leader velocity from initiation site to termination time-resolved with 3D interferometry," *J. Geophys. Res., Atmos.*, vol. 126, no. 9, Dec. 2020, Art. no. e2020JD034309, doi: 10.1002/essoar.10505017.1.
- [34] T. Morimoto and Z. Kawasaki, "VHF broadband digital interferometer," IEEJ Trans. Electr. Electron. Eng., vol. 1, no. 2, pp. 140–144, Aug. 2006, doi: 10.1002/tee.20030.
- [35] H. Liu, S. Qiu, and W. Dong, "The three-dimensional locating of VHF broadband lightning interferometers," *Atmosphere*, vol. 9, no. 8, p. 317, Aug. 2018, doi: 10.3390/atmos9080317.
- [36] X. Shao et al., "Broadband RF interferometric mapping and polarization (BIMAP) observations of lightning discharges: Revealing new physics insights into breakdown processes," *J. Geophys. Res.*, Atmos., vol. 123, no. 18, pp. 10326–10340, Sep. 2018, doi: 10.1029/2018jd029096.
- [37] X. Fan et al., "Radio interferometer observations and analysis of an energetic in-cloud pulse based on ensemble empirical mode decomposition," *IEEE Trans. Geosci. Remote Sens.*, vol. 60, 2022, Art. no. 2001017, doi: 10.1109/TGRS.2021.3078738.
- [38] X. Fan, P. R. Krehbiel, M. A. Stanley, W. Rison, H. E. Edens, and Y. Zhang, "An improved method for analyzing broadband VHF interferometer lightning observations," *IEEE Trans. Geosci. Remote Sens.*, vol. 61, 2023, Art. no. 2003218, doi: 10.1109/TGRS.2023.3299368.



Xiangpeng Fan received the B.S. degree in atmospheric sciences from Lanzhou University, Lanzhou, China, in 2008, the M.Sc. degree in atmospheric physics from the Cold and Arid Regions Environment and Engineering Research Institute, Chinese Academy of Sciences, Lanzhou, in 2011, and the Ph.D. degree in atmospheric sciences from the Chinese Academy of Sciences, Beijing, China, in 2019.

He is currently an Associate Professor with the Department of Plateau Atmospheric Physics, Northwest Institute of Eco-Environment and Resources,

Chinese Academy of Sciences, Lanzhou. His research interests include lightning physics and lightning detection.



Paul R. Krehbiel received the B.S. and M.S. degrees in electrical engineering (with a physics option) from the Massachusetts Institute of Technology, Cambridge, MA, USA, in 1963 and 1966, respectively, and the Ph.D. degree in physics from the University of Manchester Institute of Science and Technology, Manchester, U.K., in 1982.

He is currently a Professor of physics with the Physics Department and the Langmuir Laboratory for Atmospheric Research, New Mexico Institute of Mining and Technology, Socorro, NM, USA.



Mark A. Stanley received the B.S. degree in physics from Purdue University, West Lafayette, IN, USA, in 1991, the M.S. degree in astrophysics from Michigan State University, East Lansing, MI, USA, in 1992, and the Ph.D. degree in atmospheric physics from the New Mexico Institute of Mining and Technology, Socorro, NM, USA, in 2000.

He is currently a Senior Research Specialist with the Langmuir Laboratory for Atmospheric Research, New Mexico Institute of Mining and Technology. His research interests include the design and oper-

ation of remote sensing systems, electrical discharge physics, software development, and large dataset analysis.



Yijun Zhang received the B.Sc. degree in physics from Hebei Normal University, Shijiazhuang, Hebei, China, in 1986, and the M.Sc. and Ph.D. degrees in atmospheric physics from the Cold and Arid Regions Environment and Engineering Research Institute, Chinese Academy of Sciences, Lanzhou, China, in 1989 and 1998, respectively.

He is currently a Professor with the Department of Atmospheric and Oceanic Sciences and the Institute of Atmospheric Sciences, Fudan University, Shanghai, China. His research interests include

atmospheric electricity, lightning physics, and thunderstorm electricity.



William Rison received the B.S. degree in physics from the University of Wyoming, Laramie, WY, USA, in 1973, and the Ph.D. degree in physics from the University of California at Berkeley, Berkeley, CA, USA, in 1980.

After a post-doctoral position at the Scripps Institution of Oceanography, San Diego, CA, USA, he joined the Langmuir Laboratory for Atmospheric Research, New Mexico Institute of Mining and Technology, Socorro, NM, USA, in 1984, where he is currently a Research Professor of electrical engineering.



Harald E. Edens received the M.S. degree in physics from the University of Amsterdam, Amsterdam, The Netherlands, in 2001, and the Ph.D. degree in atmospheric physics from the New Mexico Institute of Mining and Technology, Socorro, NM, USA, in 2011.

He is currently the Director of the Langmuir Laboratory for Atmospheric Research, a research division of the New Mexico Institute of Mining and Technology. His research interests are lightning physics, lightning mapping, imaging techniques, and instrument design.